nature communications

Article

https://doi.org/10.1038/s41467-025-60852-9

Suppressing electron–phonon coupling for narrow-band emitting Eu(II)-based perovskitoids

Received: 5 February 2025

Accepted: 4 June 2025

Published online: 01 July 2025

Check for updates

Kai Han[1], Xuesong Wang[2], Jiance Jin[3], Shuai Zhang[1], Liang Li[1], Yuzhen Wang[1], Lixin Ning[2] ✉ & Zhiguo Xia[1,3] ✉

Narrow-band emitters are essential for solid-state lighting, displays, and single-photon sources. Here we design a family of lead-free Eu(II)-based hybrid perovskitoids with tightly face-shared connected $[EuBr_6]^{4-}$ octahedrons, and the experimental and theoretical analyses verify that the electron-phonon coupling therein is suppressed via symmetrical structural parameters as confirmed by the low Huang–Rhys factor, and thus diminishes the homogeneous broadening of the emission bandwidths. Thus, $TEtEuBr_3$ (TEt is Tetraethylammoniumwith) with symmetrical octahedrons shows ultra-narrow-band cyan emission (full width at half maximum ~36 nm) characterized by localized 5*d*-4*f* transition of Eu(II). The as-fabricated phosphor-converted light-emitting-diodes demonstrate low blue light hazard index and high color-rendering index of 96% in full-spectrum lighting technologies, moreover, they realize ultrahigh color gamut of ~115% Rec. 2020 as four-color display devices. We expect this strategy can be expanded to other narrow-band emitters for state-of-the-art optoelectronic applications.

Lead halide perovskites (LHPs), $APbX_3$ (A = Cs, methylammonium MA, formamidinium FA; X = Cl, Br, I), continue to receive immense attention as burgeoning narrow-band emitters (NBEs) for optoelectronic devices, such as light-emitting diodes (LEDs), super-resolution imaging, and quantum light sources[1–4]. The emission bandwidth (EMW) of NBEs is of prime importance for improving efficiency of light sources and color purity of high-definition display[5–7]. Thanks to the narrow EMW with the full width at half-maximum (FWHM) of <40 nm, LHPs can be the access to opportunity for entering display market[8–10]. Especially, research progress in EMW of full-inorganic $CsPbX_3$ and hybrid $FAPbBr_3$ nano-crystals is a prompter for LPHs as single-photon sources facilitated by charged exciton fast nonradiative Auger decay[11,12]. However, the luminescence efficiency of LHPs single-photon sources plummets with EMW dwindling. Additionally, there remain issues with lead toxicity and unsatisfactory stability of LHPs.

Lead-free rare-earth Eu(II)-based perovskitoids (EuPs) have been developed recently as creating an alternative class of NBEs profited from strongly localized Eu^{2+}-bound excitons and low phonon frequencies (~ 200 cm^{-1})[13–15]. They feature fortunate thermal stability and ultrahigh external quantum efficiency (Φ_{EQE}) of photoluminescence of over 50%. Yet, further suppression of EMW in EuPs remains a formidable challenge because the mechanism behind the small EMW is not well understood[16–19]. The relationship between the structure and the EMW at the microscopic level is critical to achieve ultra-narrow EuP-based emitters for state-of-the-art optoelectronic devices. Theoretically, the broadening of emission band is originated from

[1]State Key Laboratory of Luminescent Materials and Devices, Guangdong Provincial Key Laboratory of Fiber Laser Materials and Applied Techniques, Guangdong Engineering Technology Research and Development Center of Special Optical Fiber Materials and Devices, School of Physics and Optoelectronics, South China University of Technology, Guangzhou 510641, China. [2]Anhui Province Key Laboratory for Control and Applications of Optoelectronic Information Materials, Key Laboratory of Functional Molecular Solids, Ministry of Education, Anhui Normal University, Wuhu 241000, China. [3]School of Materials Science and Engineering, South China University of Technology, Guangzhou 510641, China. ✉e-mail: ninglx@mail.ahnu.edu.cn; xiazg@scut.edu.cn

inhomogeneous distribution of emission centers (inhomogeneous broadening) and the coupling with phonon vibrations in an excited electronic state (e.g., exciton) that shifts adiabatic potentials from the ground electronic state (Fig. 1a)[20]. The latter is an intrinsic property for a single emission center, and refers to as so-called the Franck–Condon shift (FCs), described by homogeneous broadening (Fig. 1a)[18,21,22]. Since the FCs is associated with lattice relaxation in the excited electronic state, and it can be strongly suppressed by tightly-connected coordination polyhedrons. It is therefore possible to reduce the EMW in self-activated EuPs by designing Eu(II) ions in tightly connected polyhedrons with uniform structural characteristics (Fig. 1b).

Here we design and employ five organic cations with distinct electrostatic potential (ESP) to dictate the structures of Eu(II)-halide polyhedrons. All of as-prepared EuPs consist of Eu octahedrons in face-shared connected pattern. The $TEtEuBr_3$, characterized with more symmetrical Eu-Br octahedrons, displays highly efficient and thermally stable ultra-narrow-band cyan emission (FWHM ~ 36 nm, Φ_{EQE} ~ 59%, 93%@120 °C). By first-principles density-functional-theory calculations, the origin of the very small EMW in $TEtEuBr_3$ is elucidated in terms of suppressed electron–phonon coupling. Accordingly, the phosphor-converted light-emitting diodes (pc-LEDs) have been fabricated and demonstrate low blue light hazard index (one-sixth of traditional white LEDs) and superior performances, including high color-rendering index of 96% in the lighting technology and larger color gamut of ~ 115% Rec. 2020 for display applications.

Results

Design of Eu(II)-based perovskitoids

We sought to design tightly-connected Eu(II)-halide polyhedrons by engaging five bulky organic ammonium molecules (Tetraethylammoniumwith TEt, triethylmethylammonium MeEt, Benzyltriethylammonium ByEt, 1-propenyl-3-methylimidazolium Emim, 1-ethyl-3-methylimidazolium Pmim) with different alkyl chains, phenyls and imidazoles (Fig. 2a). The electrostatic potential (ESP) of organic molecules were calculated (lower panel of Fig. 2a), indicating the electron-withdrawing ability of the vacant *p* orbital of nitrogen atom and iminazole/benzene units containing π–π interactions[23,24]. Moreover, the alkylamine groups (TEt and MeEt) exhibit stronger and more homogeneously symmetrical electron affinity, resulting in an increased barrier for distorted Eu-centered local structures.

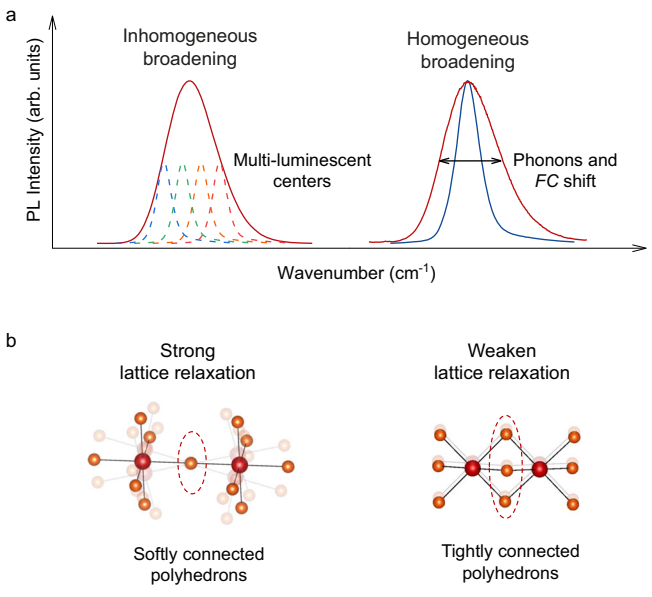

Fig. 1 | The emission broadening mechanism. a Schematics of broadening mechanisms for the EMW with homogeneous broadening and inhomogeneous broadening. **b** Schemes of structural relaxations for softly/tightly-connected coordination polyhedrons.

Therefore, we obtained single crystals of several Eu(II)-based perovskitoids (see the Experimental Section for details) and the crystal data were obtained by performing single-crystal X-ray diffraction (SCXRD measurements (details and crystal cell parameters are provided in Supplementary Tables 1, 2), namely $TEtEuBr_3$, $MeEtEuBr_3$, $ByEtEuBr_3$, $EmimEuBr_3$, $Pmim_2EuBr_4$ (Fig. 2b and Supplementary Fig. 1). Importantly, the compounds contain face-shared $[EuBr_6]^{4-}$ octahedrons isolated by organic molecules (Fig. 2c), forming one-dimensional (1D) perovskitoid structures except for 0D $Pmim_2EuBr_4$ (Fig. 2b). This sort of face-shared structures showcase strong coupling between $[EuBr_6]^{4-}$ octahedrons and good structural rigidity[25]. In particular, the 1D perovskitoid structures possess higher rigidity over the 0D one, as evidenced by the shorter Eu–Eu metallic bonding in 1D chains (3.945–4.005 Å) than in 0D clusters (4.033 Å) (Fig. 2c). Besides, we characterized powder X-ray diffraction (PXRD) patterns of all compounds to ensure their high purity (Supplementary Fig. 2).

Photoluminescence characterizations of Eu(II)-based perovskitoids

To evaluate effects of organic molecules on emission behaviors, we studied photoluminescence (PL) and photoluminescence excitation (PLE) spectra (Supplementary Fig. 3) of as-prepared Eu(II)-based perovskitoids. All compounds exhibit narrow-band cyan emissions peaking at about 490 nm (Fig. 3a). The Eu(II)-based perovskitoids with alkylamine groups display narrower EMWs than those including heterogeneous iminazole/benzene units, for example, $TEtEuBr_3$ (FWHM ~ 36 nm) versus $Pmim_2EuBr_4$ (FWHM ~ 50 nm). This suggests that 1D perovskitoid structures are more beneficial than 0D perovskitoid structures for decreasing excited-state structural relaxation and hence reducing the EMW. The narrow-band cyan emissions are ascribed to localized $5d$–$4f$ transitions of six-coordinated Eu(II)[26], as also authenticated by PL decay times of 610–750 ns (Supplementary Fig. 4). Furthermore, PL internal/external quantum efficiency (Φ_{IQE}/Φ_{EQE}) measurements (Fig. 3b and Supplementary Figs. 5 and 6) show that $TEtEuBr_3$ exhibits higher PL efficiencies (Φ_{IQE} ~ 96%, Φ_{EQE} ~ 59%) than those of other EuPs (Supplementary Table 3). Moreover, the emission intensity of $TEtEuBr_3$ remains 93% of that at room temperature when increasing temperature up to 120 °C, showing excellent thermal stability (Fig. 3c). Interestingly, the $TEtEuBr_3$ establishes relatively good air stability (PL intensity above 80% after 6 h) under humidity of 50% (Supplementary Fig. 7). Thus, $TEtEuBr_3$ displays superior PL performance in optoelectronic device applications, which could be connected with its characteristic 1D perovskitoid structures.

The time-resolved photoluminescence (TRPL) of as-prepared Eu(II)-based perovskitoids revealed a similarly narrow-band cyan emission and PL decay times without extra emission peaks (Fig. 3d and Supplementary Tables 4, 5). Moreover, the FWHMs of as-prepared Eu(II)-based perovskitoids were measured by summarizing average values of FWHMs (20 samples) (Fig. 3e), and under variable excitation wavelengths, frequencies, and power (Fig. 3f). The FWHMs are nearly unchanged, consistent with the PL results (Fig. 3a), indicating that narrow-band emission of as-prepared EuPs demonstrates strong anti-interference performance.

Mechanisms of narrow-band emission in Eu(II)-based perovskitoids

As mentioned, distribution of emission sits and lattice relaxation in the excited electronic state caused by electron–phonon coupling contribute to inhomogeneous and homogeneous broadening of the emission band, respectively. To evaluate the influence of inhomogeneous site distribution, the FWHMs for narrow-band cyan EuPs including the five compounds under study and those reported previously were collected[14,27], and the FWHM variation versus the number

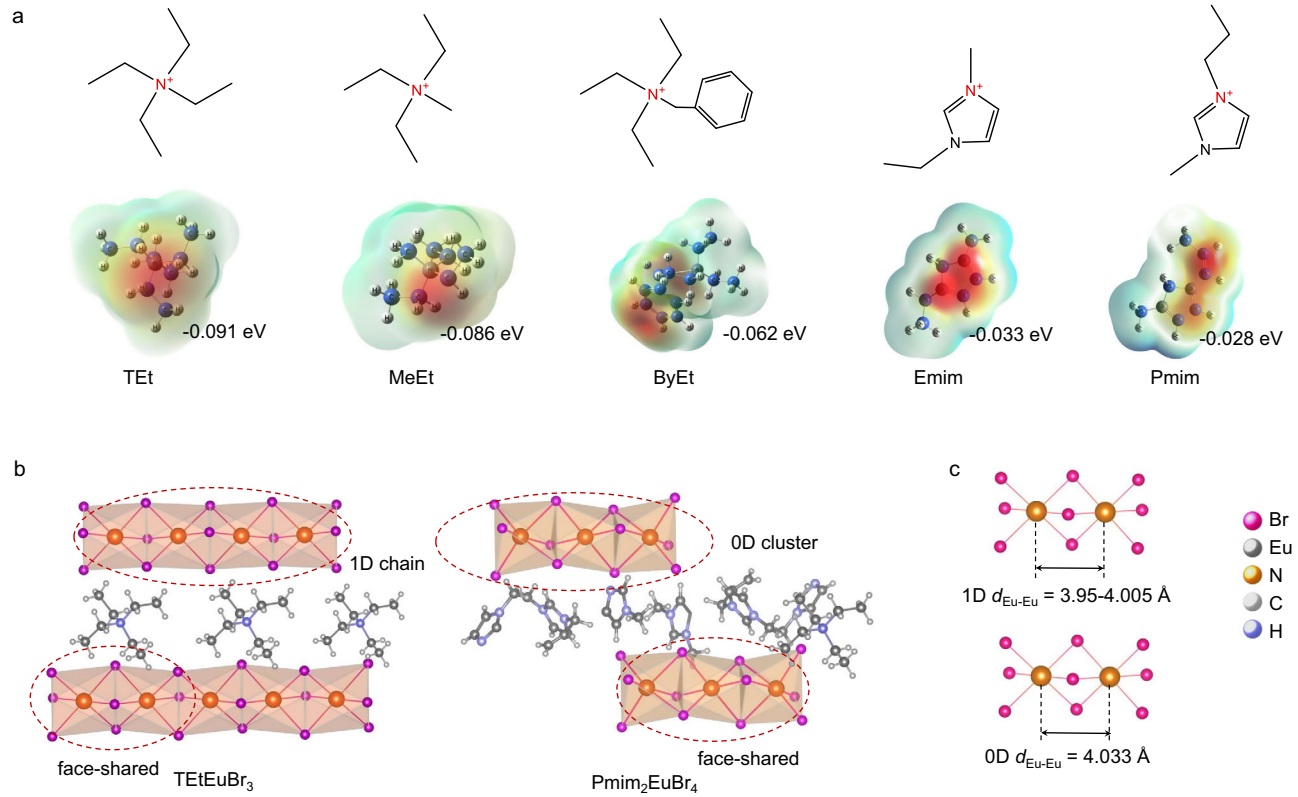

Fig. 2 | Structural design of narrow-band Eu(II)-based perovskitoids. **a** Molecular structures (upper panel) and electrostatic potential (lower panel) of organic cations (Tetraethylammoniumwith TEt (color bar, −0.091-0.091 eV), triethylmethylammonium MeEt (color bar, −0.086–0.086 eV), Benzyltriethylammonium ByEt (color bar, −0.062–0.062 eV), 1-propenyl-3-methylimidazolium Emim (color bar, −0.033–0.033 eV), 1- ethyl-3-methylimidazolium Pmim (color bar, −0.028–0.028 eV)). **b** Crystal structures of $TEtEuBr_3$ and $Pmim_2EuBr_4$ perovskitoids plotted using VESTA. **c** Local connection patterns of face-shared $[EuBr_6]^{4-}$ octahedrons in as-prepared Eu(II)-based perovskitoids. Carbon, hydrogen, nitrogen, bromine and europium are shown in dark gray, light gray, nattier blue, purple and pink, respectively.

of crystallographically distinct Eu(II) sites is depicted in Fig. 4a. There is no clear correlation between the FWHM and the Eu(II) site number, implying that the site difference is not large enough to affect the FWHM. This point is also supported by the stable singly emission peak observed in TRPL under variable excitation wavelengths, frequencies, or power.

As for the contribution of homogeneous broadening to the EMW, we first collected the structural characteristics of each distinct $[EuBr_6]^{4-}$ octahedrons in the five EuPs, in terms of the distortion index (Δd) to characterize the deviation in bond lengths, and the bond angle variance (σ^2) to quantify the distortion in bond angles[28]. The results are displayed in Fig. 4b, showing that the overall polyhedral distortion in $TEtEuBr_3$ is the smallest, in line with the narrowest EMW observed for this compound. Note that 0D $Pmim_2EuBr_4$ with soft structure exhibits the largest variation in Δd. Thus, more symmetrical Eu(II) sites bring about smaller excited-state lattice relaxation resulting in narrower emission bands.

Next, the temperature dependence of the FWHM of the emission band was investigated by using the classical equation from low-temperature PL measurements (Supplementary Fig. 8)[22,29]

$$\mathrm{FWHM}(T) = 2.36\sqrt{S}\hbar\omega\sqrt{\coth\frac{\hbar\omega}{2kT}} \quad (1)$$

where S is Huang–Rhys (H-R) factor describing electron–phonon coupling strength, ħω is the phonon vibrational frequency, k is the Boltzmann constant, and T is temperature. By fitting the above expression to the measured temperature-dependent FWHMs (Supplementary Fig. 9a), we found that the H-R factor is the smallest for $TEtEuBr_3$ (S = 1.66), in agreement with the above structural analysis. Interestingly, the derived H-R factors exhibit a positive correlation with ESPs of the organic molecules in the five compounds (Fig. 4c). Thus, organic molecules with stronger and more homogeneously symmetrical ESPs produce face-shared $[EuBr_6]^{4-}$ octahedrons with higher local symmetries, leading to weaker electron–phonon coupling and hence smaller EBWs. Moreover, $TEtEuBr_3$ displays the smallest variation of the emission peak wavelength with temperature (Supplementary Fig. 9b), indicating again its high structural rigidity. The thermal quenching activation energy for $TEtEuBr_3$ was estimated to be 187.6 meV which is the highest among the five compounds (Supplementary Fig. 9c), in consistence with its high PL efficiency.

To delve into the intricacies of the microscopic mechanism behind the small EMW, we conducted explicit calculations on the electron–phonon coupling for $TEtEuBr_3$. Hybrid DFT calculations in the 1×1×2 supercell model (containing 528 atoms with 16 Eu atoms) were performed on the structural and electronic properties, with the lowest excited electronic state being simulated by constraining the occupancies of the DFT eigenlevels. The density of states (DOS) for the ground and excited electronic state shows that the valence band top and the conduction band bottom are composed of Eu(II)-4*f* and 5*d* orbitals (Supplementary Fig. 10a), respectively, and the promotion of an electron from occupied 4*f* to empty 5*d* eigenlevels results in the appearance of an occupied 5*d* state inside the band gap (Supplementary Fig. 10b). Charge densities projected onto the 4*f*-hole and the 5*d*-electron states reveals that both states are mostly localized on the same Eu(II) center (Supplementary Fig. 11), reflecting the strong electron-hole attraction. The attraction energy was calculated to be $E_{attr} = E(GS) + E_g - E(ES) = 0.63$ eV, where $E_g = 3.48$ eV is the

https://doi.org/10.1038/s41467-025-60852-9

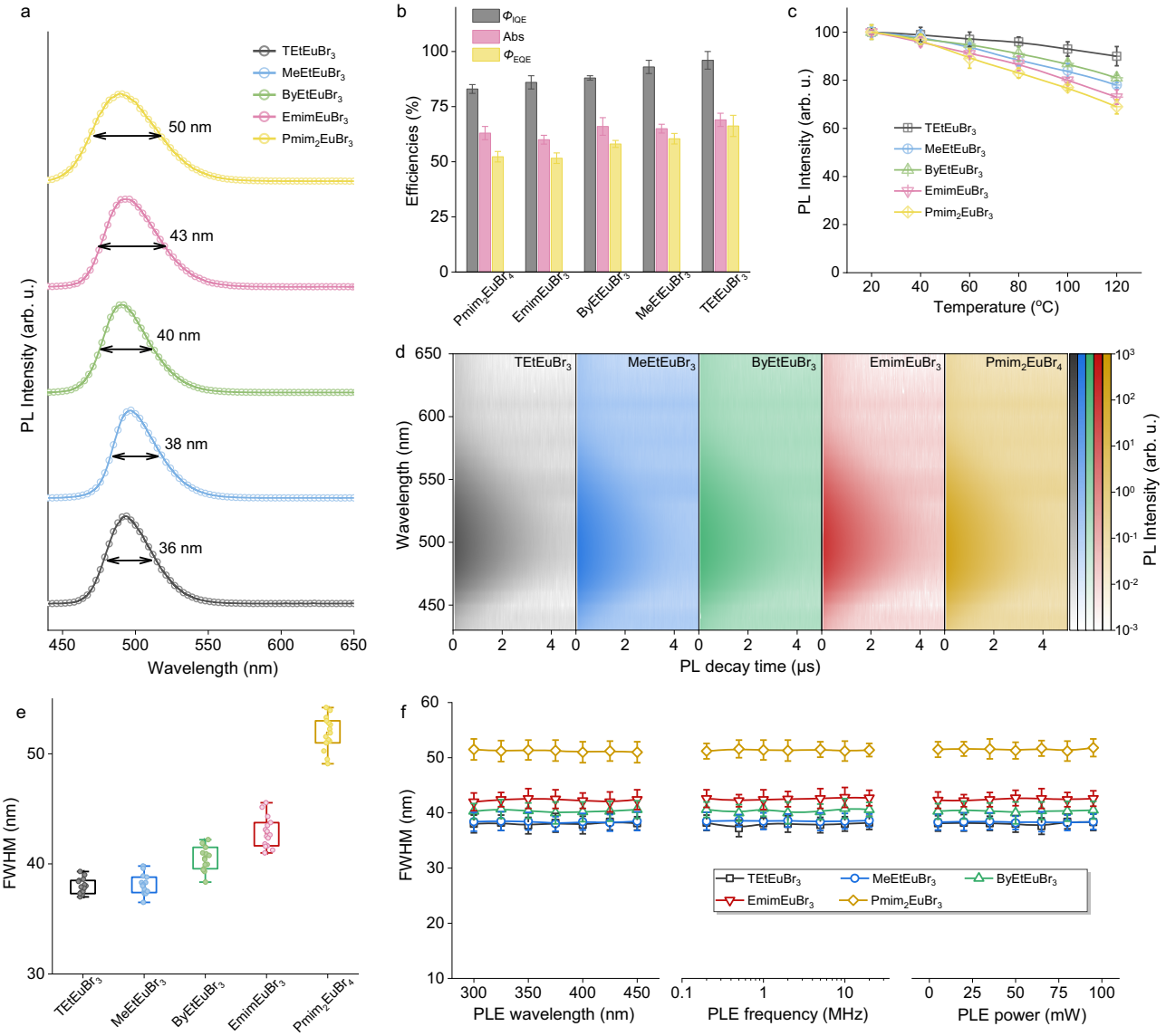

Fig. 3 | Photoluminescence of narrow-band Eu(II)-based perovskitoids. **a** Normalized PL spectra at room temperature. **b** PL internal/external quantum efficiency (Φ_{IQE}/Φ_{EQE}) and absorption efficiency (Abs), (the error bar, ±5%, from three measurements). **c** Temperature-dependent emission intensity with temperature range of 20–120 °C. **d** The time-resolved photoluminescence of $TEtEuBr_3$, $MeEtEuBr_3$, $ByEtEuBr_3$, $EmimEuBr_3$, $Pmim_2EuBr_4$ under 340 nm pulse laser diode excitation, where the *x*-axis is the PL decay time of each emission wavelength, *y*-axis is emission wavelength with spacing of 10 nm, the depth of color represents PL intensity (color bar, 10^{-3}–10^{3} arb.u.). **e** The FWHM of as-prepared Eu(II)-based perovskitoids by summarizing average values of 15 samples. **f** The full width at half maximum (FWHM) of as-prepared Eu(II)-based perovskitoids under variable excitation wavelengths (300–450 nm), frequencies (0.2–20 MHz) and power (5–100 mW) with 375 nm laser, (the error bar, ±3 nm, from five samples).

fundamental bandgap energy, and *E*(GS) and *E*(ES) are the ground and unrelaxed excited electronic state energies, respectively. The narrow-band emission in the EuP, therefore, is originated from 5*d*–4*f* transitions localized on individual Eu(II) centers.

The calculated FCs for the ground ($E_{FC,g}$) and excited ($E_{FC,e}$) electronic states of $TEtEuBr_3$ are 0.059 eV and 0.138 eV, respectively (Fig. 4d). The excited-state potential energy landscape is steeper than that of the ground state, showing larger crystal-field interaction of the 5*d* electron than of the 4*f* electrons, which is beneficial for narrowing the emission band. Figure 4e and Supplementary Fig. 12 depict atomic-position rearrangements in the excited electronic state (point C in Fig. 4d) relative to the ground electronic state (point D in Fig. 4d). The structural changes are mainly concentrated on the 6 coordinating Br atoms and the two adjacent Eu atoms, with the Eu–Br bond lengths and Eu–Eu distances shortened by 0.055–0.065 Å and 0.068 Å, respectively (Fig. 4f). Therefore, the equilibrium structure in the excited electronic state in $TEtEuBr_3$ differs little from that in the ground electronic state, which is conductive to generating the narrow band emission.

We calculated the lattice vibrations of the $TEtEuBr_3$ supercell, and the atom-projected phonon density of states are shown in the upper panel of Fig. 4g. The phonon frequency distribution agrees well with experimental Raman spectrum (lower panel of Fig. 4g). It shows that the Eu(II)- and Br-associated vibrations lie in the low frequency range of 0–150 cm^{-1}. Similar behaviors were observed for the other four compounds (Supplementary Fig. 13). By projecting the atomic-position rearrangements from the ground to the excited electronic state onto the phonon eigenvectors, the contribution of each phonon mode to the structural change were evaluated, as described by H-R factors (lower panel of Fig. 3h). The largest H-R factors (1.12, 0.53 and 0.36) are associated the phonon modes involving mainly the motions of Eu(II) and Br atoms with frequencies of 104.4 cm^{-1} (upper panel of

https://doi.org/10.1038/s41467-025-60852-9

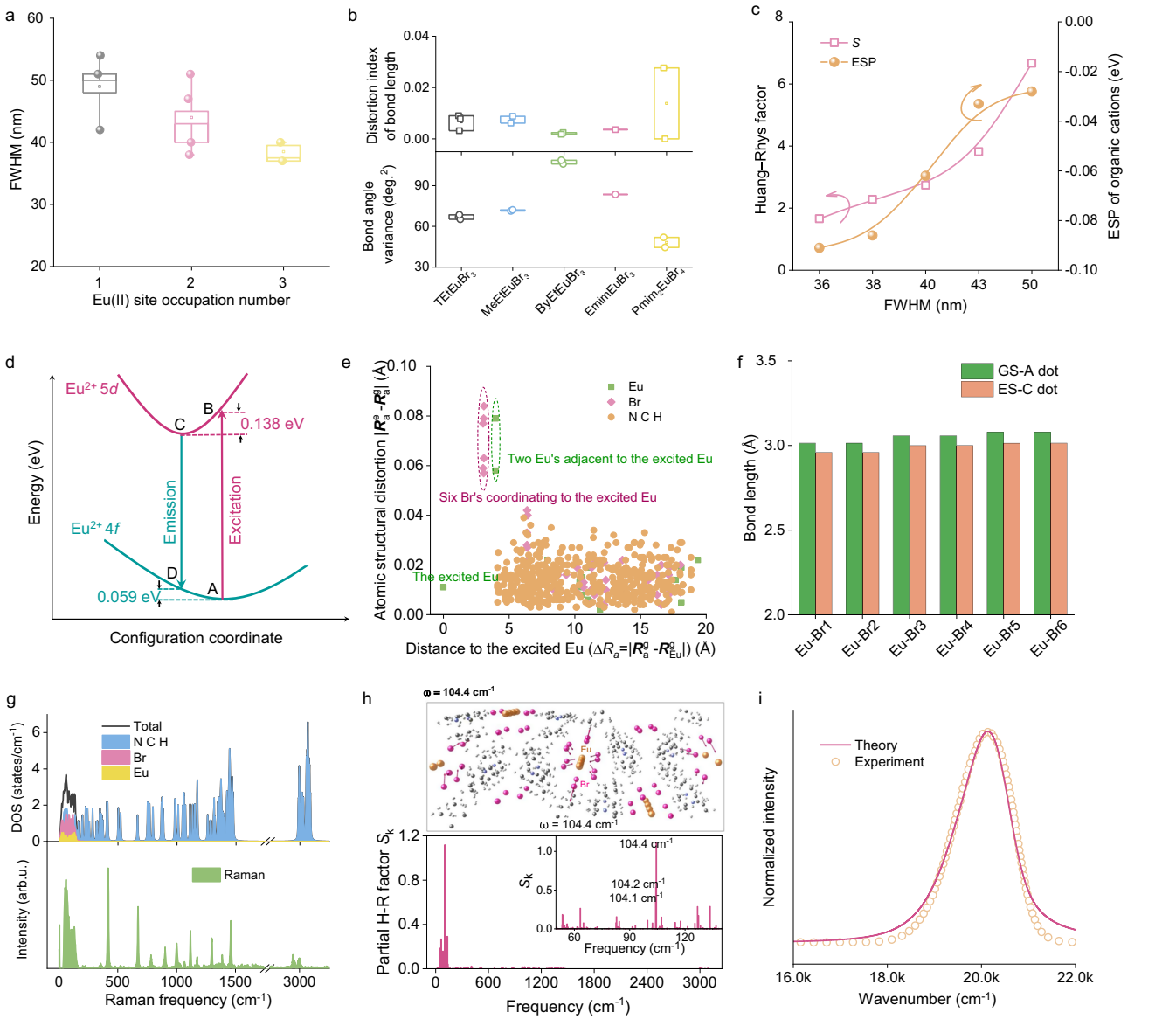

Fig. 4 | Mechanisms of narrow-band emission. a The number of crystallographically distinct Eu(II) sites dependent full width at half maximum (FWHM) for narrow-band cyan Eu(II)-based perovskitoids. **b** The distortion index (Δd) and the bond angle variance (σ^2) of polyhedral distortion in $TEtEuBr_3$. **c** Huang–Rhys factor (S), FWHM and electrostatic potential (ESP). **d** The one-dimensional configurational coordinate model of $TEtEuBr_3$ with ground state (A, D dots) and excited state (B, C dots). **e** The coordinate position change of each atom in $TEtEuBr_3$ at the excited state relative to the ground state. **f** The bond length change of Eu-Br in $TEtEuBr_3$ at the excited state (ES-C dot) relative to the ground state (GS-A dot). **g** Calculated vibrational density of states (DOS) (upper panel) and Raman spectrum (lower panel) in the experiment for $TEtEuBr_3$. **h** The distribution map of calculated Huang–Rhys factor. **i** Calculated emission spectrum compared with the experimental result. The calculated curve was shifted to align its maximum with that of the experimental emission spectrum for better comparison.

Fig. 4h), 104.2 cm^{-1}, and 104.1 cm^{-1}, respectively (Supplementary Fig. 14). With the calculated H-R factors, the emission band shape was calculated by the generating function approach, and a good agreement with the experimental data is shown in Fig. 4i. These results support that $TEtEuBr_3$ is characterized with low electron–phonon coupling, giving rise to ultra-narrow-band emission.

LEDs for lighting and display by Eu(II)-based perovskitoids

Despite extensive efforts to improve efficiency and color purity in recent decades, existing LEDs cannot be reconfigured to meet harmless light source due to service of blue excitation source[30]. For instance, the most potent bule region (446–477 nm) suppresses melatonin in healthy human subjects, inducing circadian-phase shifting or autonomic stimulation[31]. Herein, we construct a white pc-LED device (LED3) using $TEtEuBr_3$ with the commercial phosphors (YAG:Ce^{3+} and K_2SiF_6:Mn^{4+}) embedding into NUV InGaN LED chips (λ = 405 nm) to evaluate the practical performance as harmless light source (Fig. 5a). By comparison with two commercial consulting solutions of white pc-LEDs, i.e., blue (LED1) /NUV (LED2) LEDs combining to phosphors (YAG:Ce^{3+} and K_2SiF_6:Mn^{4+}), LED3 has an excellent color render index (R_a = ~96), a color temperature (CCT) of 6243 K, CIE color coordinate (0.311, 0.341), as well as lower blue light hazard index (L_λ of ~one-sixth of traditional white LEDs) (Fig. 5b and Supplementary Fig. 15a). It can act as harmless light source for full-spectrum lighting. Additionally, LED3 also exhibits good fatigue life and stability, with unchanged emission intensity after 500 h of continuous operation (Fig. 5c).

Moreover, $TEtEuBr_3$, as an innovated narrow-band emitter, represents an attractive candidate for wide color gamut display. We proposed and fabricated four-color LED devices with the green-emitting Eu(II) hybrids, commercial red phosphor K_2SiF_6:Mn^{4+} and a

https://doi.org/10.1038/s41467-025-60852-9

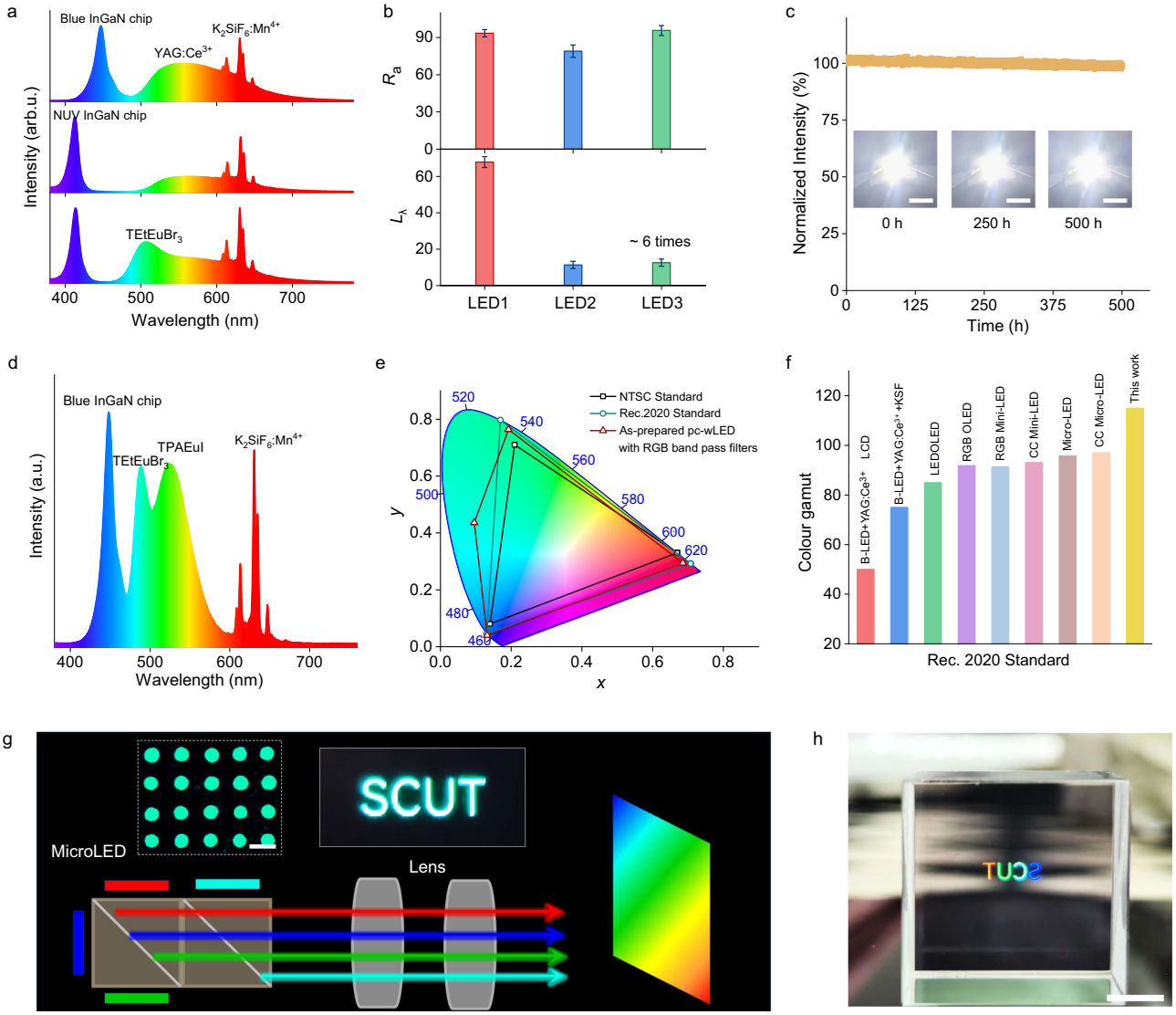

Fig. 5 | Applications in LED devices. a The emission spectra of white LED1, LED2 and LED3 devices at a current of 20 mA. **b** The color render index (R_a) and light hazard index (L_λ) of white LED1, LED2 and LED3 devices, (the error bar, ±4, from three LED devices). **c** The fatigue life and stability of LED3 device, the inset is photograph of LED3 (scale bar, 5 mm). **d** The emission spectra of four-color LED device. **e** Chromaticity (x, y) of as-fabricated four-color LED device with RGB band pass filters in comparison with Rec. 2020. **f** Comparison of color gamut for as-prepared four-color LED device and commercial LED display screens. **g** Schematic diagram of color mixing technique for four-color display, the inset is fluorescence microscopy picture of as-prepared micro-LED (scale bar, 10 μm) plotted using Microsoft PowerPoint. **h** The imaging of four-color display by as-prepared micro-LED display screen with light up four-color emission "SCUT" (scale bar, 1 cm).

450 nm blue InGaN chip. Figure 5d displays the emission spectrum of the LED device under a current of 50 mA, obtaining high luminous efficacy of 102 lm W^{-1}, CCT ~ 7280 K and CIE color coordinate (0.303, 0.298) (Supplementary Fig. 15b). Benefitting from expanded four-color display technology, the four-color LED device achieves an ultrahigh color gamut of 115% Rec. 2020 standard (Fig. 5e), which is superior to the state-of-the-art LED display technologies, including OLED, CC Mini-LED, and Micro-LED[5,32], as shown in Fig. 5f. Additionally, we fabricated pc-LED devices using $TEtEuBr_3$ and commercial narrow-band phosphors (β-SiAlON:Eu^{2+} and $BaSi_2O_2N:Eu^{2+}$) for comparison, as shown in Supplementary Fig. 16. The pc-LED using $TEtEuBr_3$ reaches a high photoelectric efficiency of ~25% at 20 mA, and excellent long-term operational stability (>96% after 600 h), thermal stability (>90% @ 120 °C), and humidity stability (Supplementary Figs. 17–19). Taking advantage of characteristics of solution-processed $TEtEuBr_3$, we fabricated micro cyan conversion layers in quartz panels with pixel size ~5 μm (inset of Fig. 5g). By color mixing technique (Fig. 5g), four-color display image "SCUT" is illustrated, as shown in Fig. 5h.

In summary, we develop lead-free Eu(II)-based perovskitoids as a burgeoning family of narrow-band emitters. The emission bandwidths have been decreased via employing rigid face-shared connected $[EuBr_6]^{4-}$ octahedrons, and the suppressed electron–phonon coupling contributes to reduce the homogeneous broadening of Eu(II) therein. Typically, $TEtEuBr_3$ with symmetrical octahedrons accomplishes ultra-narrow-band cyan emission (FWHM ~ 36 nm). The as-fabricated pc-LEDs show a lower blue light hazard index (one-sixth of traditional white LEDs), with superior performance (high color-rendering index of 96% as full-spectrum white light sources and larger color gamut of ~ 115% Rec. 2020) for four-color display devices. Our results open an untapped avenue to design and tailored narrow-band emitters for state-of-the-art optoelectronic applications.

Methods

Synthesis of $TEtEuBr_3$, $MeEtEuBr_3$, $TEtEuBr_3$, and $EmimEuBr_3$ perovskitoids

A total of 1 mmol of $EuBr_2$ (99.5%, Grirem Advanced Materials Co. Ltd.) and 1 mmol of the corresponding organic molecule (tetraethylammonium bromide, triethylmethylammonium bromide, benzyltriethylammonium bromide, or 1-propenyl-3-methylimidazolium bromide; 99%, Alfa Aesar) were combined with 3–6 mL of anhydrous methanol (99.7%, Macklin) in a 10 mL Pyrex bottle. The mixture was heated to 60 °C under continuous stirring for 1 h to obtain a homogeneous solution. Subsequently, the bottle was placed in a glovebox for crystal growth via slow evaporation at room temperature. Iridescent single crystals formed after one week. All manipulations were conducted in a nitrogen-filled glovebox with H_2O and O_2 levels maintained below 0.1 ppm.

Synthesis of $Pmim_2EuBr_4$ perovskitoids

For the synthesis of $Pmim_2EuBr_4$ perovskitoids, 1 mmol of $EuBr_2$ (99.5%, China Grinm Group Co. Ltd.) and 2 mmol of 1-ethyl-3-methylimidazolium bromide (99%, Alfa Aesar) were mixed and sealed in a vacuum quartz tube at approximately 5×10^{-4} Pa (Partulab device, MRVS-1002). The sealed quartz tubes were heated to 230 °C for 12 h and then cooled to 25 °C at a rate of 3 °C h^{-1} to obtain single crystals. All procedures were performed in a nitrogen-filled glovebox with H_2O and O_2 levels maintained below 0.1 ppm.

Fabrication of pc-LEDs

The fabrication of pc-LEDs involved several configurations: LED1 was created by adding commercial phosphors (YAG:Ce^{3+} and K_2SiF_6:Mn^{4+}) onto a blue LED chip (λ_{max} = 450 nm). LED2 was assembled using the same commercial phosphors (YAG:Ce^{3+} and K_2SiF_6:Mn^{4+}) on near-ultraviolet (NUV) InGaN LED chips (λ = 405 nm). LED3 was fabricated by incorporated $TEtEuBr_3$ along with commercial phosphors (YAG:Ce^{3+} and K_2SiF_6:Mn^{4+}) on NUV InGaN LED chips (λ_{max} = 405 nm). A four-color LED device was fabricated by combining $TEtEuBr_3$ with green-emitting Eu(II) hybrids and the commercial red phosphor K_2SiF_6:Mn^{4+} on a 450 nm blue InGaN chip.

Characterization

Single-crystal X-ray diffraction was conducted using an XtaLAB Synergy R X-ray single-crystal diffractometer equipped with a hybrid pixel array detector and a Mo Kα radiation source (λ = 0.71073 Å) at 150 K. The structures were solved by direct methods and refined using full-matrix least squares on F^2 using the SHELX-2018 program package. Crystallographic data and details of structural refinements are provided in Supplementary Tables 1, 2. The Cambridge Crystallographic Data Centre has assigned CCDC numbers 2405465 ($ByEtEuBr_3$) [https://doi.org/0.5517/ccdc.csd.cc2lr2n3], 2405465 [https://doi.org/0.5517/ccdc.csd.cc2lr2n3], 2405466 ($Pmim_2EuBr_4$) [https://doi.org/0.5517/ccdc.csd.cc2lr2p4], 2405467 ($MeEtEuBr_3$) [https://doi.org/0.5517/ccdc.csd.cc2lr2q5], 2405468 ($TEtEuBr_3$) [https://doi.org/0.5517/ccdc.csd.cc2lr2r6], 2405469 ($EmimEuBr_3$) [https://doi.org/0.5517/ccdc.csd.cc2lr2s7], these supplementary crystallographic data can be obtained free of charge from www.ccdc.cam.ac.uk/data_request/cif.

Powder X-ray diffraction (XRD) data were collected using a D8 Advance diffractometer with Cu Kα radiation (λ = 1.541862 Å) at room temperature, operating at 40 kV and 15 mA.

Photoluminescence excitation (PLE), photoluminescence (PL), photoluminescence quantum yield, and PL decay spectra were measured using an FLS1000 fluorescence spectrophotometer (Edinburgh Instruments). The PL spectra, color-rendering index (R_a), and correlated color temperature (CCT) of the fabricated pc-LEDs were collected using an integrating sphere spectroradiometer system (ATA-1000, Everfine).

Computational methods

The $TEtEuBr_3$ crystal was modeled by a periodic 1 × 1 × 2 supercell containing 528 atoms. The antiferromagnetic arrangement between adjacent $Eu^{2+}(4f^7)$ ions along the 1D chain was adopted, which was found to be more energetically stable than the ferromagnetic arrangement. The structural and electronic properties of the supercell in the ground and excited electronic states were calculated by periodic DFT with the hybrid HSE06 functional[33,34], while the phonon vibration eigenvalues and eigenvectors were calculated with the PBE + U method[35–37], as implemented in the VASP package[38,39]. The electrons of Eu ($5s^25p^64f^76s^2$), Br($4s^24p^6$), N($2s^22p^3$), C($2s^22p^2$), and H($1s^1$) were treated as valence electrons, and their interactions with the respective cores were described by the projected augmented wave (PAW) method[40]. The geometry optimizations were performed until the total energies and the forces on the atoms converged to 10^{-6} eV and 0.01 eV $Å^{-1}$, respectively. Due to the large size of the supercell, one k-point Γ was adopted to sample the Brillouin zone and the cutoff energy for the plane wave basis was set to 430 eV.

The emission bandshape for an electronic transition can be written as $I(\omega) = C\omega^3 A(\omega)$, where C is the normalization factor, ω is the angular frequency and $A(\omega)$ is the lineshape function. The lineshape function can be calculated using the generating function approach under the Franck-Condon and parallel-mode approximations, provided that only the lowest vibrational level of the excited electronic state is occupied such as at low temperatures[41–44]. The lineshape function is expressed as

$$A(E_{ZPL} - \hbar\omega) = \frac{1}{2\pi}\int_{-\infty}^{\infty} G(t)e^{i\omega t - \gamma t}dt \quad (2)$$

where γ is a parameter representing homogeneous broadening and E_{ZPL} is the transition energy of the zero-phonon line. $G(t)$ is the generating function given by $G(t) = e^{S(t)-S(0)}$, where $S(t)$ is the Fourier transformation of the spectral function $S(\omega)$, given by

$$S(\omega) = \sum\nolimits_k S_k \delta(\omega - \omega_k) \quad (3)$$

where S_k is the partial Huang-Rhys (H-R) factor of the phonon mode with frequency ω. In the present study, the δ-function was approximated by a normalized Lorentzian function with width 240 cm^{-1}. It can be expressed as $S_k = \frac{1}{2\hbar}\omega_k(\triangle Q_k)^2$, where the coordinate difference $\triangle Q_k$ is defined as

$$\triangle Q_k = \sum\nolimits_a \sqrt{m_a}(R_a^e - R_a^g)\cdot u_{k,a} \quad (4)$$

m_a is the mass of atom a, R_a^e and R_a^g are the equilibrium positions of atom a in the excited and ground electronic states, and $u_{k,a}$ is the displacement vector of atom a in the phonon mode k.

Data availability

The data that support the findings of this study are available from the corresponding author upon request. Source data are provided with this paper. The supplementary crystallographic data can be obtained free of charge from www.ccdc.cam.ac.uk/data_request/cif. Source data are provided with this paper.

References

1. Kovalenko, M. V., Protesescu, L. & Bodnarchuk, M. I. Properties and potential optoelectronic applications of lead halide perovskite nanocrystals. *Science* **358**, 745–750 (2017).
2. Hassan, Y. et al. Ligand-engineered bandgap stability in mixed-halide perovskite LEDs. *Nature* **591**, 72–77 (2021).
3. Fu, Y. et al. Metal halide perovskite nanostructures for optoelectronic applications and the study of physical properties. *Nat. Rev. Mater.* **4**, 169–188 (2019).

4. Rainò, G. et al. Superfluorescence from lead halide perovskite quantum dot superlattices. *Nature* **563**, 671–675 (2018).
5. Huang, Y., Hsiang, E.-L., Deng, M.-Y. & Wu, S.-T. Mini-LED, Micro-LED and OLED displays: present status and future perspectives. *Light Sci. Appl.* **9**, 105 (2020).
6. Zhao, M., Zhang, Q. & Xia, Z. Narrow-band emitters in LED backlights for liquid-crystal displays. *Mater. Today* **40**, 246–265 (2020).
7. Song, J. et al. Quantum dot light-emitting diodes based on inorganic perovskite cesium lead halides ($CsPbX_3$). *Adv. Mater.* **27**, 7162–7167 (2015).
8. Yang, X. et al. Towards micro-PeLED displays. *Nat. Rev. Mater.* **8**, 341–353 (2023).
9. Shamsi, J., Urban, A. S., Imran, M., De Trizio, L. & Manna, L. Metal halide perovskite nanocrystals: synthesis, post-synthesis modifications, and their optical properties. *Chem. Rev.* **119**, 3296–3348 (2019).
10. Wu, X.-g, Ji, H., Yan, X. & Zhong, H. Industry outlook of perovskite quantum dots for display applications. *Nat. Nanotechnol.* **17**, 813–816 (2022).
11. Utzat, H. et al. Coherent single-photon emission from colloidal lead halide perovskite quantum dots. *Science* **363**, 1068–1072 (2019).
12. Rainò, G. et al. Ultra-narrow room-temperature emission from single $CsPbBr_3$ perovskite quantum dots. *Nat. Commun.* **13**, 2587 (2022).
13. Han, K. et al. Narrow-Band Green-Emitting Hybrid Organic–Inorganic Eu (II)-Iodides for Next-Generation Micro-LED Displays. *Adv. Mater.* **36**, 2313247 (2024).
14. Han, K. et al. Hybrid Eu(II)-bromide scintillators with efficient 5*d*-4*f* bandgap transition for X-ray imaging. *Light Sci. Appl.* **13**, 222 (2024).
15. Luo, J. et al. Efficient blue light emitting diodes based on europium halide perovskites. *Adv. Mater.* **33**, 2101903 (2021).
16. Wang, L., Xie, R.-J., Suehiro, T., Takeda, T. & Hirosaki, N. Down-conversion nitride materials for solid state lighting: recent advances and perspectives. *Chem. Rev.* **118**, 1951–2009 (2018).
17. Zhao, M. et al. Next-generation narrow-band green-emitting $RbLi(Li_3SiO_4)_2:Eu^{2+}$ phosphor for backlight display application. *Adv. Mater.* **30**, 1802489 (2018).
18. Pust, P. et al. Narrow-band red-emitting $Sr[LiAl_3N_4]:Eu^{2+}$ as a next-generation LED-phosphor material. *Nat. Mater.* **13**, 891–896 (2014).
19. Yang, L. et al. Efficient deep-blue electroluminescence from Ce-based metal halide. *Nat. Commun.* **15**, 6240 (2024).
20. Nguyen, H. A. et al. Design rules for obtaining narrow luminescence from semiconductors made in solution. *Chem. Rev.* **123**, 7890–7952 (2023).
21. Dey, M. & Singh, A. K. Broad photoluminescence from large Frank-Condon relaxation dynamics of hole polarons in $LiGaO_2$. *Phys. Rev. B* **108**, L041201 (2023).
22. Jia, Y., Poncé, S., Miglio, A., Mikami, M. & Gonze, X. Beyond the one-dimensional configuration coordinate model of photoluminescence. *Phys. Rev. B* **100**, 155109 (2019).
23. Chen, H. et al. Improved charge extraction in inverted perovskite solar cells with dual-site-binding ligands. *Science* **384**, 189–193 (2024).
24. Liu, C. et al. Two-dimensional perovskitoids enhance stability in perovskite solar cells. *Nature* **633**, 359–364 (2024).
25. Guan, D. et al. Exceptionally robust face-sharing motifs enable efficient and durable water oxidation. *Adv. Mater.* **33**, 2103392 (2021).
26. Dorenbos, P. Thermal quenching of Eu2+ 5d–4f luminescence in inorganic compounds. *J. Phys.-Condens Matter* **17**, 8103 (2005).
27. Jin, J., Han, K., Wang, Y. & Xia, Z. Bandgap narrowing in europium(II)-based bromide hybrids toward improved X-ray scintillation and imaging. *Chem. Mater.* **36**, 4813–4820 (2024).
28. Mao, L. et al. Structural diversity in white-light-emitting hybrid lead bromide perovskites. *J. Am. Chem. Soc.* **140**, 13078–13088 (2018).
29. Alkauskas, A., Lyons, J. L., Steiauf, D. & Van de Walle, C. G. First-principles calculations of luminescence spectrum line shapes for defects in semiconductors: the Example of GaN and ZnO. *Phys. Rev. Lett.* **109**, 267401 (2012).
30. Françon, A., Behar-Cohen, F. & Torriglia, A. The blue light hazard and its use on the evaluation of photochemical risk for domestic lighting. An in vivo study. *Environ. Int.* **184**, 108471 (2024).
31. Pattison, P. M., Tsao, J. Y., Brainard, G. C. & Bugbee, B. LEDs for photons, physiology and food. *Nature* **563**, 493–500 (2018).
32. Liu, Z. et al. Micro-light-emitting diodes with quantum dots in display technology. *Light Sci. Appl.* **9**, 83 (2020).
33. Perdew, J. P., Ernzerhof, M. & Burke, K. Rationale for mixing exact exchange with density functional approximations. *J. Chem. Phys.* **105**, 9982–9985 (1996).
34. Krukau, A. V., Vydrov, O. A., Izmaylov, A. F. & Scuseria, G. E. Influence of the exchange screening parameter on the performance of screened hybrid functionals. *J. Chem. Phys.* **125**, 224106 (2006).
35. Dudarev, S. L., Botton, G. A., Savrasov, S. Y., Humphreys, C. J. & Sutton, A. P. Electron-energy-loss spectra and the structural stability of nickel oxide: an LSDA+U study. *Phys. Rev. B* **57**, 1505–1509 (1998).
36. Canning, A., Chaudhry, A., Boutchko, R. & Grønbech-Jensen, N. First-principles study of luminescence in Ce-doped inorganic scintillators. *Phys. Rev. B* **83**, 125115 (2011).
37. Perdew, J. P., Burke, K. & Ernzerhof, M. Generalized gradient approximation made simple. *Phys. Rev. Lett.* **77**, 3865–3868 (1996).
38. Kresse, G. & Furthmüller, J. Efficient iterative schemes for ab initio total-energy calculations using a plane-wave basis set. *Phys. Rev. B* **54**, 11169–11186 (1996).
39. Kresse, G. & Joubert, D. From ultrasoft pseudopotentials to the projector augmented-wave method. *Phys. Rev. B* **59**, 1758–1775 (1999).
40. Blöchl, P. E. Projector augmented-wave method. *Phys. Rev. B* **50**, 17953–17979 (1994).
41. Lax, M. The Franck-Condon principle and its application to crystals. *J. Chem. Phys.* **20**, 1752–1760 (1952).
42. Kubo, R. & Toyozawa, Y. Application of the method of generating function to radiative and non-radiative transitions of a trapped electron in a crystal. *Prog. Theor. Phys.* **13**, 160–182 (1955).
43. Miyakawa, T. & Dexter, D. L. Phonon sidebands, multiphonon relaxation of excited states, and phonon-assisted energy transfer between ions in solids. *Phys. Rev. B* **1**, 2961–2969 (1970).
44. Linderälv, C., Åberg, D. & Erhart, P. Luminescence quenching via deep defect states: a recombination pathway via oxygen vacancies in Ce-doped YAG. *Chem. Mater.* **33**, 73–80 (2021).

Acknowledgements

This research was supported by National Natural Science Foundations of China (52425206, 22361132525, 12474398), and China Postdoctoral Science Foundation (No. 2024M760954).

Author contributions

X.Z.G. and H.K. conceived and planned the work. H.K., J.J.C. and L.L. prepared the samples and processed the experimental data. X.Z.G., H.K., Z.S, and W.Y.Z. interpreted the theoretical and experimental results. N.L.X. and W.X.S. performed the DFT calculations and revised the paper. H.K. wrote the paper, X.Z.G. supervised the work. All authors discussed and edited the paper.

Competing interests

The authors declare no competing interests

Additional information

Supplementary information The online version contains supplementary material available at https://doi.org/10.1038/s41467-025-60852-9.

Correspondence and requests for materials should be addressed to Lixin Ning or Zhiguo Xia.

Peer review information *Nature Communications* thanks Chih Shan Tan, Jiajun Luo and the other anonymous, reviewer(s) for their contribution to the peer review of this work. A peer review file is available.